Perturbation theory for modeling galaxy bias: Validation with simulations of the Dark Energy Survey

S. Pandey,[1] E. Krause,[2] B. Jain,[1] N. MacCrann,[3,4] J. Blazek,[3,5] M. Crocce,[6,7] J. DeRose,[8,9] X. Fang,[2,10] I. Ferrero,[11] O. Friedrich,[12] M. Aguena,[13,14] S. Allam,[15] J. Annis,[15] S. Avila,[16] G. M. Bernstein,[1] D. Brooks,[17] D. L. Burke,[18,19] A. Carnero Rosell,[20,21] M. Carrasco Kind,[22,23] J. Carretero,[24] M. Costanzi,[25,26] L. N. da Costa,[14,27] J. De Vicente,[28] S. Desai,[29] J. Elvin-Poole,[3,4] S. Everett,[9] P. Fosalba,[6,7] J. Frieman,[15,30] J. García-Bellido,[16] D. Gruen,[31,18,19] R. A. Gruendl,[22,23] J. Gschwend,[14,27] G. Gutierrez,[15] K. Honscheid,[3,4] K. Kuehn,[32,33] N. Kuropatkin,[15] M. A. G. Maia,[14,27] J. L. Marshall,[34] F. Menanteau,[22,23] R. Miquel,[35,24] A. Palmese,[15,30] F. Paz-Chinchón,[36,23] A. A. Plazas,[37] A. Roodman,[18,19] E. Sanchez,[28] V. Scarpine,[15] M. Schubnell,[38] S. Serrano,[6,7] I. Sevilla-Noarbe,[28] M. Smith,[39] M. Soares-Santos,[38] E. Suchyta,[40] M. E. C. Swanson,[23] G. Tarle,[38] and J. Weller[41,42]

(DES Collaboration)

[1]*Department of Physics and Astronomy, University of Pennsylvania, Philadelphia, Pennsylvania 19104, USA*
[2]*Department of Astronomy/Steward Observatory, University of Arizona, 933 North Cherry Avenue, Tucson, Arizona 85721-0065, USA*
[3]*Center for Cosmology and Astro-Particle Physics, The Ohio State University, Columbus, Ohio 43210, USA*
[4]*Department of Physics, The Ohio State University, Columbus, Ohio 43210, USA*
[5]*Institute of Physics, Laboratory of Astrophysics, École Polytechnique Fédérale de Lausanne (EPFL), Observatoire de Sauverny, 1290 Versoix, Switzerland*
[6]*Institut d'Estudis Espacials de Catalunya (IEEC), 08034 Barcelona, Spain*
[7]*Institute of Space Sciences (ICE, CSIC), Campus UAB, Carrer de Can Magrans, s/n, 08193 Barcelona, Spain*
[8]*Department of Astronomy, University of California, Berkeley, 501 Campbell Hall, Berkeley, California 94720, USA*
[9]*Santa Cruz Institute for Particle Physics, Santa Cruz, California 95064, USA*
[10]*Department of Physics, University of Arizona, Tucson, Arizona 85721, USA*
[11]*Institute of Theoretical Astrophysics, University of Oslo, P.O. Box 1029 Blindern, NO-0315 Oslo, Norway*
[12]*Kavli Institute for Cosmology, University of Cambridge, Madingley Road, Cambridge CB3 0HA, United Kingdom*
[13]*Departamento de Física Matemática, Instituto de Física, Universidade de São Paulo, CP 66318, São Paulo, SP, 05314-970, Brazil*
[14]*Laboratório Interinstitucional de e-Astronomia—LIneA, Rua General José Cristino 77, Rio de Janeiro, RJ, 20921-400, Brazil*
[15]*Fermi National Accelerator Laboratory, P.O. Box 500, Batavia, Illinois 60510, USA*
[16]*Instituto de Fisica Teorica UAM/CSIC, Universidad Autonoma de Madrid, 28049 Madrid, Spain*
[17]*Department of Physics & Astronomy, University College London, Gower Street, London, WC1E 6BT, United Kingdom*
[18]*Kavli Institute for Particle Astrophysics & Cosmology, P.O. Box 2450, Stanford University, Stanford, California 94305, USA*
[19]*SLAC National Accelerator Laboratory, Menlo Park, California 94025, USA*
[20]*Instituto de Astrofisica de Canarias, E-38205 La Laguna, Tenerife, Spain*
[21]*Universidad de La Laguna, Departamento Astrofisica, E-38206 La Laguna, Tenerife, Spain*
[22]*Department of Astronomy, University of Illinois at Urbana-Champaign, 1002 West Green Street, Urbana, Illinois 61801, USA*
[23]*National Center for Supercomputing Applications, 1205 West Clark Street, Urbana, Illinois 61801, USA*
[24]*Institut de Física d'Altes Energies (IFAE), The Barcelona Institute of Science and Technology, Campus UAB, 08193 Bellaterra (Barcelona), Spain*
[25]*INAF—Osservatorio Astronomico di Trieste, via Giovanni Battista Tiepolo 11, I-34143 Trieste, Italy*
[26]*Institute for Fundamental Physics of the Universe, Via Beirut 2, 34014 Trieste, Italy*
[27]*Observatório Nacional, Rua General José Cristino 77, Rio de Janeiro, RJ, 20921-400, Brazil*
[28]*Centro de Investigaciones Energéticas, Medioambientales y Tecnológicas (CIEMAT), Madrid, Spain*

[29]*Department of Physics, IIT Hyderabad, Kandi, Telangana 502285, India*
[30]*Kavli Institute for Cosmological Physics, University of Chicago, Chicago, Illinois 60637, USA*
[31]*Department of Physics, Stanford University, 382 Via Pueblo Mall, Stanford, California 94305, USA*
[32]*Australian Astronomical Optics, Macquarie University, North Ryde, New South Wales 2113, Australia*
[33]*Lowell Observatory, 1400 Mars Hill Road, Flagstaff, Arizona 86001, USA*
[34]*George P. and Cynthia Woods Mitchell Institute for Fundamental Physics and Astronomy, and Department of Physics and Astronomy, Texas A&M University, College Station, Texas 77843, USA*
[35]*Institució Catalana de Recerca i Estudis Avançats, E-08010 Barcelona, Spain*
[36]*Institute of Astronomy, University of Cambridge, Madingley Road, Cambridge CB3 0HA, United Kingdom*
[37]*Department of Astrophysical Sciences, Princeton University, Peyton Hall, Princeton, New Jersey 08544, USA*
[38]*Department of Physics, University of Michigan, Ann Arbor, Michigan 48109, USA*
[39]*School of Physics and Astronomy, University of Southampton, Southampton, SO17 1BJ, United Kingdom*
[40]*Computer Science and Mathematics Division, Oak Ridge National Laboratory, Oak Ridge, Tennessee 37831, USA*
[41]*Max Planck Institute for Extraterrestrial Physics, Giessenbachstrasse, 85748 Garching, Germany*
[42]*Universitäts-Sternwarte, Fakultät für Physik, Ludwig-Maximilians Universität München, Scheinerstrasse 1, 81679 München, Germany*

(Received 23 September 2020; accepted 18 November 2020; published 8 December 2020)

We describe perturbation theory (PT) models of galaxy bias for applications to photometric galaxy surveys. We model the galaxy-galaxy and galaxy-matter correlation functions in configuration space and validate against measurements from mock catalogs designed for the Dark Energy Survey (DES). We find that an effective PT model with five galaxy bias parameters provides a good description of the 3D correlation functions above scales of 4 Mpc$/h$ and $z < 1$. Our tests show that at the projected precision of the DES Year 3 analysis, two of the nonlinear bias parameters can be fixed to their coevolution values, and a third (the k^2 term for higher derivative bias) set to zero. The agreement is typically at the 2% level over scales of interest, which is the statistical uncertainty of our simulation measurements. To achieve this level of agreement, our *fiducial* model requires using the full nonlinear matter power spectrum (rather than the one-loop PT one). We also measure the relationship between the nonlinear and linear bias parameters and compare them to their expected coevolution values. We use these tests to motivate the galaxy bias model and scale cuts for the cosmological analysis of the Dark Energy Survey; our conclusions are generally applicable to all photometric surveys.

DOI: 10.1103/PhysRevD.102.123522

I. INTRODUCTION

The structure in the Universe at low redshift was seeded by small perturbations in the early Universe. Although the evolution of these tiny perturbations is well described in the linear regime, their nonlinear evolution on small scales is an active area of research.

There is a well-formulated framework of nonlinear perturbative expansions of these early fluctuations in both Eulerian and Lagrangian space (see Refs. [1] and [2] for a review). Major approaches include standard perturbation theory (SPT) [3,4], Lagrangian perturbation theory (LPT) [5,6], renormalized perturbation theory [7], and effective field theory (EFT) [8–10]. Although these theories analytically describe the relation between dark matter nonlinear density perturbations and linear density perturbations, direct observations exist only for some biased tracers of the underlying dark matter field. These theories have therefore been extended to describe biased tracers like galaxies [6,11–17] and applied to data [18–25].

Another analytical approach for biased tracers is the halo model framework (see Ref. [26] for a review). The halo model assumes that all matter is bound in virialized objects (halos) and relates clustering statistics to halos. This framework can be extended to include the observed tracers—for example, via the halo occupation distribution (HOD) [27,28]. However, unlike the perturbation theory, the parametrization of the HOD is tracer dependent and cannot be easily generalized [29,30]. Moreover, the HOD only describes the distribution of galaxies inside halos (known as the one-halo term). To correctly describe the clustering of galaxies on weakly nonlinear scales, between the nonlinear one-halo regime and the large-scale linear regime, would require a combination with perturbative models.

Several studies have tested the perturbation theory (PT) of biased tracers in Fourier space (mostly focused on redshift surveys) [31–35]. This study focuses on PT in configuration space using standard perturbation theory (SPT) and effective field theory (EFT). We use the 3D

correlation functions, ξ_{gg} and ξ_{gm}, constructed from galaxy and matter catalogs built from simulations. One of the key results of our analysis is the minimum length scale for which the correlation functions can be modeled with PT.

The mock catalogs used in this analysis are designed for the Dark Energy Survey (DES). As described in Sec. III, our focus is on Year 3 (Y3) DES datasets, for which we use the mocks to validate our PT models. This dataset constitutes the largest current imaging survey of galaxies, and thus careful testing and validation that match its statistical power are essential for extracting information in the nonlinear regime. We also project the 3D correlations from mocks to the angular correlations (as measured by photometric surveys), but since projection results in loss of information, our 3D tests are more stringent. Since the PT formalism is not tied to any particular tracer, and the scales of interest are well above the one-halo regime (where differences in galaxy assignment schemes matter), we expect that our conclusions will have broad validity for the lensing and galaxy clustering analyses from imaging surveys.

We also aim to test the accuracy of different variants of perturbation theory for cosmological applications with DES. Although this analysis is at fixed cosmology, we implement fast evaluations of the projected correlations so that they can feasibly be used for cosmological parameter analysis. Finally, we explore the possibility of placing well-motivated priors on some of the PT bias parameters.

This paper is organized as follows: In Sec. II, we review the existing perturbation theory literature and the models used in this study. Section III describes the simulations used for the measurements, and Sec. IV describes the analysis choices. The results are presented in Sec. V, and we conclude in Sec. VI.

II. FORMALISM

We summarize in this section the perturbation theory formalism used in our study and the projected two-point statistics relevant for surveys like DES. We are interested in modeling both the matter and galaxy distributions. Different perturbation theory approaches describe the evolved galaxy density fluctuations $\delta_g(\mathbf{x})$ of a biased tracer, g, in terms of the linear matter density fluctuations $\delta_L(\mathbf{x})$. Although formally the relationship between $\delta_g(\mathbf{x})$ and $\delta_L(\mathbf{x})$ is on the full past Lagrangian path of a particle at Eulerian position $\mathbf{x}$, in this analysis we use the approximation that this relationship is instantaneous, meaning $\delta_g(\mathbf{x}, z)$ is related only to $\delta_L(\mathbf{x}, z)$ at any redshift z.

A. Standard perturbation theory

Standard perturbation theory expands the evolved dark matter density field $\delta_m(\mathbf{x})$ in terms of the extrapolated linear density field, shear field, the divergence of the velocity field, and rotational invariants constructed using the gravitational potential. In Fourier space, this expansion can be written as [1]

$$\delta_m(\mathbf{k}) = \sum \frac{1}{n!} \int \frac{d^3k_1}{(2\pi)^3} \cdots \frac{d^3k_n}{(2\pi)^3} (2\pi)^3 \delta_D(\mathbf{k}_{1\ldots n} - \mathbf{k}) F_n \times (\mathbf{k}_1, \ldots, \mathbf{k}_n) \delta_L(\mathbf{k}_1) \ldots \delta_L(\mathbf{k}_n). \quad (1)$$

Here $F_n(\mathbf{k}_1, \ldots, \mathbf{k}_n)$ are the mode coupling kernels constructed out of correlations between the scalar quantities mentioned above, and δ_D is the Dirac delta function. The form of the F_n kernels can be derived by solving the perturbative fluid equations. For example, under the assumptions of the spatially flat, cold dark matter model of cosmology, F_2 is well approximated by

$$F_2(\mathbf{k}, \mathbf{k}') = \left[(1+\alpha) + \mu \left(\frac{k}{k'} + \frac{k'}{k} \right) + (1-\alpha)\mu^2 \right]. \quad (2)$$

For $\Omega_m < 1$, $\alpha = \frac{3}{7} (\Omega_m)^{-2/63}$ and $\mu = \frac{\mathbf{k}\cdot\mathbf{k}'}{k \cdot k'}$. In this analysis, we use the Einstein–de Sitter limit and assume $\alpha = \frac{3}{7}$.

1. Biased tracers

The overdensity of biased tracers is modeled as the sum of a deterministic function of the dark matter density ($f[\delta_m(\mathbf{x})]$) and a stochastic component [$\varepsilon(\mathbf{x})$] [36–38]:

$$\delta_g(\mathbf{x}) = f[\delta_m(\mathbf{x})] + \varepsilon(\mathbf{x}). \quad (3)$$

Given the galaxy sample and scales of our interest (which are greater than the Lagrangian radius of the host halos of our galaxy sample) in this analysis, we ignore the stochastic contribution and focus on the deterministic relation between the dark matter field and the biased tracer. Assuming a local biasing scheme, this expansion is given as [4]

$$\delta_g^{\text{local}}(\mathbf{x}) = \sum_{n=1}^{\infty} \frac{b_n}{n!} \delta_m^n(\mathbf{x}). \quad (4)$$

However, as is well known [11,14], on small scales this local biasing in Eulerian space rapidly breaks down. Assuming isotropy and homogeneity, the bias parameters have to be scalar, and hence the density of a tracer can only depend on scalar quantities [15]. Therefore, nonlocal terms can only be sourced by scalar quantities constructed out of gravitational evolution of matter density (δ_m), shear ($\nabla_i \nabla_j \Phi$), and velocity divergences ($\nabla_i v_j$). Following the procedure in Refs. [15,39,40], these contributions can be rearranged into independent terms that contribute to the overdensity of galaxies (δ_g) at different orders:

$$\delta_g \sim f(\delta_m, \nabla_i\nabla_j\Phi, \nabla_i v_j) \sim f^{(1)}(\delta_m) + f^{(2)}(\delta_m^2, s^2) + f^{(3)}(\delta_m^3, \delta_m s^2, \psi, st) + \cdots. \quad (5)$$

Here f^i are the functions that contribute to the total overdensity at ith order only, and ψ, s, and t are the scalar quantities constructed out of shear and velocity divergences. When expanding the form of these functions f^i up to third order, we introduce un-normalized bias factors as given in Eqs. (9) and (12) of McDonald and Roy [15]. In Fourier space, the equivalent equation is Eq. (A14) of Saito *et al.* [31].

B. Higher derivative bias

In the above section, the nonlocal terms included in the expansion of galaxy overdensity come only from shear and velocity divergences. However, those terms are still local in the spatial sense, meaning that the formation of biased tracers only depends on the scalar quantities discussed above at the same position as the tracer. A short-range nonlocality due to nonlinear effects in halo and galaxy formation within some scale R will change Eq. (3) as follows (according to Ref. [15]):

$$\delta_g(\mathbf{x}) = f[\delta_m(\mathbf{x}')], \quad (6)$$

where generally $|\mathbf{x} - \mathbf{x}'| < R$, and R is usually of the order of the halo radius. By Taylor-expanding this function, we can see that the lowest-order gradient-type term that can contribute to δ_g is proportional to $\nabla^2\delta_m$. Hence, we can further generalize our Eq. (5) to include this gradient-type term as

$$\delta_g \sim f(\delta_m, \nabla_i\nabla_j\Phi, \nabla_i v_j) \sim f^{(1)}(\delta_m) + f^{(2)}(\delta_m^2, s^2) + f^{(3)}(\delta_m^3, \delta_m s^2, \psi, st) + f^{\mathrm{grad}}(\nabla^2\delta_m) + \cdots. \quad (7)$$

Note that in Fourier space, this term would scale as $k^2\delta_m(k)$.

C. Effective field theory

Moreover, as discussed in Carrasco *et al.* [8], it is theoretically inconsistent to use small-scale modes in the integration over Fourier space. So, we use effective integrated ultraviolet (UV) terms in the final expansion for the power spectrum. This effective term also enters as a k^2 contribution in the large-scale limit. For example, if we expand the nonlinear matter power spectrum in terms of the linear power spectrum $[P_L(k)]$ using the PT framework, we have to include this k^2 piece usually written as $c_s^2 k^2 P_L(k)$, where c_s is the effective adiabatic sound speed.

D. Regularized PT power spectra

Note that the bias parameters that will appear in the expansion of δ_g in Eq. (7) will be unobservable "bare bias" parameters and need not have the physical meaning usually attributed to the large-scale tracer bias (for example, the measurable responses of galaxy statistics to a given fluctuation). We refer the reader to McDonald and Roy [15] for the details on the renormalization of these "bare bias" parameters by combining all the parameters with similar power spectrum kernels. After renormalizing, we can write the tracer-matter cross spectrum (P_{gm}) and autopower spectrum of the tracer (P_{gg}) as

$$P_{gm}(k) = b_1 P_{mm}(k) + \frac{1}{2} b_2 P_{b_1 b_2}(k) + \frac{1}{2} b_s P_{b_1 s^2}(k) + \frac{1}{2} b_{3nl} P_{b_1 b_{3nl}}(k) + (b^{hd}_{\nabla^2\delta} + c_s^2) k^2 P^{\mathrm{grad}}_{mm}(k), \quad (8)$$

$$P_{gg}(k) = b_1^2 P_{mm}(k) + b_1 b_2 P_{b_1 b_2}(k) + b_1 b_s P_{b_1 s^2}(k) + b_1 b_{3nl} P_{b_1 b_{3nl}}(k) + \frac{1}{4} b_2^2 P_{b_2 b_2}(k) + \frac{1}{2} b_2 b_s P_{b_2 s^2}(k) + \frac{1}{4} b_s^2 P_{s^2 s^2}(k) + b_1 (2 b^{hd}_{\nabla^2\delta} + c_s^2) k^2 P^{\mathrm{grad}}_{mm}(k). \quad (9)$$

Here, the bias parameters like b_1, b_2, b_s, and b_{3nl} are the renormalized bias parameters which are physically observable. The bias parameter $b^{hd}_{\nabla^2\delta}$ is the higher-derivative bias parameter, and c_s^2 is the sound-speed term as described by EFT (Sec. II C). As for the kernels, $P_{b_1 b_2}(k)$ is generated from the ensemble average of $\langle \delta_m \delta_m^2 \rangle$, $P_{b_1 s^2}(k)$ is generated from $\langle \delta_m s^2 \rangle$, and $P_{b_1 b_{3nl}}$ is generated from a combination of the ensemble average between δ_m and arguments of $f^{(3)}$ [see Eq. (7)] that contribute at the one-loop level [31]. For the exact form of the above kernels, see the Appendix A of Saito *et al.* [31].

Instead of expanding the Eulerian galaxy overdensity field directly as we have done above, we can also predict the galaxy overdensity by evolving the Lagrangian galaxy overdensity (see Matsubara [16] for detailed calculations). These two approaches should evaluate to the same galaxy overdensity at a given loop order [16,31,40–42]. By equating the two approaches and neglecting shear-like terms in the Lagrangian overdensity, as they are small for bias values of our interest (see Sec. V and Ref. [43]), we get the prediction of the coevolution value of the renormalized bias parameters: $b_s = (-4/7) \times (b_1 - 1)$ and $b_{3nl} = (b_1 - 1)$ [16,31].[1] This coevolution picture naturally describes how gravitational evolution generates the nonlocal biasing even from the local biased tracers in a high-redshift Lagrangian frame.

We use different choices of P_{mm} and P^{grad}_{mm} in our analysis. These choices will be detailed in Sec. IV A.

[1]Note that our coevolution value of b_{3nl} differs from that of Saito *et al.* [31], as we include their prefactor of 32/315 in our definition of $P_{b_1 b_{3nl}}$.

E. 3D statistics to projected statistics

We are interested in the cosmological applications of imaging surveys via projected correlation functions. Projections of the 3D correlation functions ξ_{gg} and ξ_{gm} to angular coordinates in finite redshift bins give the projected correlations known as $w_{gg}(\theta)$ and $\gamma_t(\theta)$, respectively. We estimate the covariance of these projected statistics for the DES-Y3-like survey. This allows us to estimate the angular scales for which our perturbation theory model is a good description for DES-Y3-like sensitivity.

1. Galaxy-galaxy clustering

The angular correlation function $w_{gg}(\theta)$ is given by the Limber integral

$$w_{gg}(\theta) = \int_0^\infty d\chi \chi^4 \phi^2(\chi) \int_{-\infty}^{\infty} dr_\parallel \xi_{gg}\left(\sqrt{r_\parallel^2 + \chi^2\theta^2}\right), \quad (10)$$

where χ is the comoving distance and $\phi(\chi)$ is the normalized radial selection function of the lens galaxies, related to the normalized redshift distribution of lens galaxies $[n_g(z)]$ as $\phi(\chi) = (1/\chi^2)(dz/d\chi)n_g(z)$.

To simplify the above equation and ones that follow, the inner integral will be denoted by $w_{gg}^p = \int_{-\infty}^{\infty} dr_\parallel \xi_{gg} \times \left(\sqrt{r_\parallel^2 + \chi^2\theta^2}\right)$. A similar equation applies for the galaxy-matter correlation as well. The integral limits for this projection integral are from $-\infty$ to ∞. Though our analysis of survey data is over a finite projection length, as described below in Sec. III, our thinnest tomographic bin spans redshift $0.3 < z < 0.45$—a distance of over 500 Mpc$/h$. Moreover, as our analysis uses true galaxy redshifts, there is no peculiar velocity effect on projected integrals [44]. Therefore, ignoring the finite bin size introduces negligible errors in our correlation function predictions.

Substituting the radial selection function in terms of the galaxy redshift distribution and using the above definition of w^p, the projected galaxy clustering, $w_{gg}(\theta)$, can be expressed as

$$w_{gg}(\theta) = \int_0^\infty dz \frac{dz}{d\chi} n_g^2(z) w_{gg}^p(\chi\theta). \quad (11)$$

2. Galaxy-galaxy lensing

The galaxy-galaxy lensing signal (γ_t) is related to the excess surface mass density ($\Delta\Sigma$) around lens galaxies by

$$\gamma_t(\theta, z_l, z_s) = \frac{\Delta\Sigma(\theta, z_l)}{\Sigma_{crit}(z_l, z_s)}, \quad (12)$$

where Σ_{crit} is the critical surface mass density given by

$$\Sigma_{crit}(z_l, z_s) = \frac{c^2}{4\pi G} \frac{D_A(z_s)}{D_A(z_l) D_A(z_l, z_s)}. \quad (13)$$

Here D_A is the angular diameter distance, z_l is the redshift of the lens, and z_s is the redshift of the source.

The surface mass density at the projected distance $r_p = \chi\theta$ can be related to the projected galaxy-matter correlation function by

$$\Sigma(r_p, z) = \langle\Sigma\rangle + \rho_m(z) w_{gm}^p(r_p, z), \quad (14)$$

where $\langle\Sigma\rangle$ is the mean surface density,

$$\langle\Sigma\rangle = \int_{z_{min}}^{z_{max}} dz \frac{d\chi}{dz} \rho_m(z), \quad (15)$$

and $\rho_m(z) = \Omega_{m,0}(1+z)^3 \rho_{crit,0}$ is the mean density of the Universe.

Therefore, the excess surface density is

$$\Delta\Sigma(r_p, z) = \rho_m(z)(\bar{w}_{gm}^p(r_p, z) - w_{gm}^p(r_p, z)) \quad (16)$$

$$= \rho_m(z) \Delta w_{gm}^p(r_p, z), \quad (17)$$

where $\bar{w}_{gm}^p(r_p, z)$ is given as

$$\bar{w}_{gm}^p(\chi\theta, z) = \frac{2}{(\chi\theta)^2} \left[\int_0^{\chi\theta} dr_p r_p w_{gm}^p(r_p, z)\right]. \quad (18)$$

Now, combining all the above equations, the galaxy-galaxy lensing signal for lenses at redshift z_l and sources at redshift z_s is

$$\gamma_t(\theta, z_l, z_s) = \frac{\Delta w_{gm}^p(\chi\theta, z_l)\rho_m(z_l)}{\Sigma_{crit}(z_l, z_s)}. \quad (19)$$

Averaging this signal with the redshift distribution of sources ($n_s(z_s)$) would give

$$\gamma_t(\theta, z_l) = \Delta w_{gm}^p(\chi\theta)\rho_m(z) \int_0^\infty dz_s n_s(z_s) \frac{1}{\Sigma_{crit}(z_l, z_s)}. \quad (20)$$

Finally, averaging this signal with the redshift distribution of lens galaxies ($n_g(z_l)$) gives

$$\gamma_t(\theta) = \int_0^\infty dz_l \rho_m(z_l) n_g(z_l) \Delta w_{gm}^p(\chi\theta) \times \int_0^\infty dz_s n_s(z_s) \frac{1}{\Sigma_{crit}(z_l, z_s)}. \quad (21)$$

The tangential shear $\gamma_t(\theta)$ is nonlocal and depends on the correlation function at all scales smaller than the transverse distance $\chi\theta$ [Eq. (18); see MacCrann *et al.* [45] and

Baldauf *et al.* [46] for a detailed analysis]. Perturbation theory is not adequate for modeling these small scales. We therefore add to γ_t a term representing a point-mass contribution: B/θ^2, where B is the average point mass for a sample of lens and source galaxies and is treated as a free parameter. Any spherically symmetric mass distribution within the minimum scale used is captured by the point-mass term, thus removing our sensitivity to these scales. Our final expression for the galaxy-galaxy lensing signal is

$$\gamma_t(\theta) = \gamma_t^{\rm theory}(\theta) + \frac{B}{\theta^2}, \tag{22}$$

with $\gamma_t^{\rm theory}$ given by Eq. (21).

III. SIMULATIONS AND MOCK CATALOGS

The full DES survey was completed in 2019 and covered ~5000 square degrees of the South Galactic Cap. Mounted on the Cerro Tololo Inter-American Observatory (CTIO) 4 m Blanco telescope in Chile, the 570 megapixel Dark Energy Camera (DECam) [47] images the field in *grizY* filters. The raw images are processed by the DES Data Management (DESDM) team [48,49]. The Year 3 (Y3) catalogs of interest for this study span the full footprint of the survey but with fewer exposures (and depth) than the complete survey. About 1×10^7 galaxies have shear and photometric redshift measurements that enable their use for cosmology. For the full details of the data and the galaxy and lensing shear catalogs, we refer the readers to Refs. [50] and [51].

We use DES-like mock galaxy catalogs from the `MICE` simulation suite in this analysis. The `MICE` Grand Challenge simulation (MICE-GC) is an N-body simulation run in a cube with side length 3 Gpc$/h$ with 4096^3 particles using the Gadget-2 code [52] with a mass resolution of $2.93 \times 10^{10}\ M_\odot/h$. Halos are identified using a friend-of-friends algorithm with linking length 0.2. For further details about this simulation, see Fosalba *et al.* [53]. These halos are then populated with galaxies using a hybrid subhalo abundance matching plus halo occupation distribution (HOD) approach, as detailed in Carretero *et al.* [54]. These methods are designed to match the joint distributions of luminosity, $g-r$ color, and clustering amplitude observed in SDSS [30]. The construction of the halo and galaxy catalogs is described in Crocce *et al.* [55]. `MICE` assumes a flat ΛCDM cosmological model with $h = 0.7$, $\Omega_m = 0.25$, $\Omega_b = 0.044$, and $\sigma_8 = 0.8$.

We use two galaxy samples generated from the full `MICE` galaxy catalog. A DES-like lightcone catalog of `redMaGiC` galaxies [56] with average photometric errors matching DES Y1 data is generated. We also use another galaxy sample (`Maglim` hereafter) based on cuts on galaxy magnitude only. This sample is created by imposing a cut on the simulated DES i-band-like magnitudes (mag-i) of `MICE` galaxies [57]. The galaxies in this `Maglim` sample follow the conditions mag-$i > 17.5$ and mag-$i < 4z + 18$, where z is the true redshift of the galaxy. This definition results from a sample optimization process when deriving cosmological information from a combined clustering and lensing analysis [57]. Both simulated galaxy samples populate one octant of the sky (ca. 5156 deg^2), which is slightly larger than the sky area of DES Y3 data (approximately 4500 deg^2 [51]). From these simulations, we measure the nonlinear bias parameters at fixed cosmology, which we use as fiducial values for the DES galaxy sample(s).

As detailed in later sections, we divide our galaxy samples into four tomographic bins with edges [0.3, 0.45, 0.6, 0.75, 0.9]. These bins are the same as the last four of the five tomographic bins used in the DES Y1 analysis [58,59]. We do not fit to the first tomographic bin of DES Y1 analysis (which is $0.15 < z < 0.3$), because we are limited by the jackknife covariance estimate (see Sec. IV D and Appendix A). These tomographic bins cover a similar redshift range as planned for the DES Y3 analysis. Note that we bin our galaxies used in this analysis using their true spectroscopic redshift. Therefore, there is no overlap in the redshift distribution of galaxies between two different bins. After all color, magnitude, and redshift cuts, there are 2.1×10^6 `redMaGiC` galaxies and 2.0×10^6 `Maglim` galaxies (downsampled to have approximately the same number density as `redMaGiC`) used in this analysis. The normalized number densities of two catalogs are shown in Fig. 1.

We note that although both the mock catalogs used in this analysis are calibrated with DES Y1 data, we do not expect our tests and conclusions to change with the Y3 mock catalog. Since our tests are based on the true redshifts of the galaxies, we are not sensitive to photometric redshift uncertainties, exact tomography choices, or color selection of the galaxies.

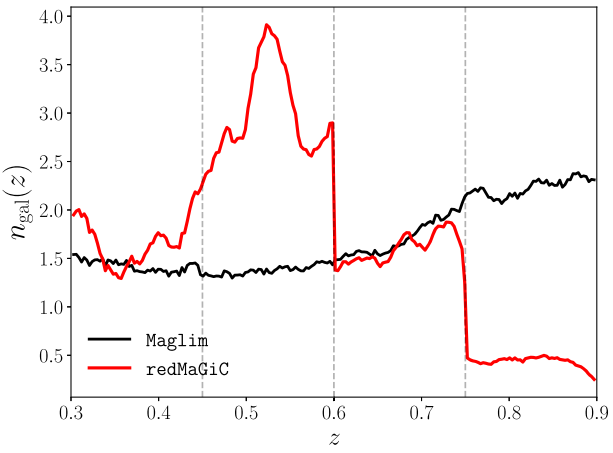

FIG. 1. Comparison of normalized number density of galaxies corresponding to `redMaGiC` and `Maglim` samples. The dashed vertical lines denote the tomographic bin edges.

TABLE I. Variations in the choice of power spectra elements in the three models considered here. Based on the analysis of the three models, we will use Model C as our *fiducial* model (see Sec. V).

Models	$P_{\rm mm}$	$P_{\rm mm}^{\rm grad}$	Remarks
Model A	$P_{\rm mm}^{\rm HF}$	0	Linear bias model
Model B	$P_{\rm mm}^{\rm 1-loop}$	$P_{\rm L}$	One-loop EFT model
Model C	$P_{\rm mm}^{\rm HF}$	$P_{\rm mm}^{\rm HF}$	*Fiducial* model

IV. ANALYSIS

A. Data vector and models

Our main analysis involves the auto- and cross-correlation functions for galaxies and matter: $\xi_{\rm mm}$, $\xi_{\rm gm}$, and $\xi_{\rm gg}$. Our focus is on galaxy bias, so we would like to minimize artifacts that are specific to the clustering of matter, in particular sampling effects due to the finite volume of the simulations (see Appendix A). Therefore, we fit our theory models to the ratios: $\xi_{\rm gg}/\xi_{\rm mm}$ and $\xi_{\rm gm}/\xi_{\rm mm}$ so that the galaxy two-point functions are analyzed relative to the matter-matter correlation (see Appendix B and Fig. 12 for an analysis on correlation functions $\xi_{\rm gm}$ and $\xi_{\rm gg}$ directly). We consider three models to describe these measured ratios:

$$\begin{aligned}
&\text{A}: \frac{\xi_{\rm gm}}{\xi_{\rm mm}} = b_1, \\
&\text{B}: \frac{\xi_{\rm gm}}{\xi_{\rm mm}} = \frac{\mathcal{F}[b_1 P_{\rm mm}^{\rm 1-loop}(k) + P_{\rm gm}^{\rm 1-Loop}(k) + k^2 b_{\nabla^2\delta} P_{\rm lin}(k)]}{\mathcal{F}[P_{\rm mm}^{\rm HF}(k)]}, \\
&\text{C}: \frac{\xi_{\rm gm}}{\xi_{\rm mm}} = \frac{\mathcal{F}[b_1 P_{\rm mm}^{\rm HF}(k) + P_{\rm gm}^{\rm 1-Loop}(k) + k^2 b_{\nabla^2\delta} P_{\rm mm}^{\rm HF}(k)]}{\mathcal{F}[P_{\rm mm}^{\rm HF}(k)]},
\end{aligned} \tag{23}$$

where, $\mathcal{F}$ denotes the Fourier transform, and $P_{\rm gm}^{\rm 1-Loop}(k)$ is the effective sum of all the terms dependent on b_2, $b_{\rm s}$, and $b_{\rm 3nl}$ in Eq. (8). An analogous form of this expansion can be derived for $P_{\rm gg}(k)$. The term $P_{\rm mm}^{\rm 1-Loop}(k)$ is the one-loop PT estimate of the matter-matter correlation function. Model A is the linear bias model, and the numerator in Model B is similar to the model considered by previous analyses using the EFT description of clustering [10,24,25,60–63]. In this study, we also analyze Model C, which differs from Model B in the use of the full nonlinear matter power spectrum using *halofit* (as opposed to the one-loop PT in Model B) in the numerator. This model is motivated by completely resumming the matter-matter autocorrelation term to all orders as it uses the fully nonlinear fits to simulations such as *halofit* [64]: $P_{\rm mm}^{\rm NL} = P_{\rm mm}^{\rm HF}$. We make a similar choice for $P_{\rm mm}^{\rm grad}(k)$ [65]. The bias term, $b_{\nabla^2\delta}$, is the sum of both the higher-derivative bias term ($b_{\nabla^2\delta}^{\rm hd}$) and the sound-speed term ($c_{\rm s}^2$) for $P_{\rm gm}(k)$. The sound-speed term is zero in Model C, as the fully nonlinear matter power spectra include any correction from the UV divergent integrals. Hence, in Model C, $b_{\nabla^2\delta} = b_{\nabla^2\delta}^{\rm hd}$. Unlike Model C, in Model B the sound-speed term is not zero, so there we denote $b_{\nabla^2\delta} = b_{\nabla^2\delta}^{\rm hd} + c_{\rm s}^2$.

The choices of different power spectra for the three models are given in Table I.

Note that the denominators of Models B and C implicitly assume that *halofit* is a good description of the matter-matter correlation on the scales we are interested in. We check this assumption using the matter density field from the MICE simulations. The residuals of the matter-matter correlation functions for both *halofit* and EFT are shown in Fig. 2. The EFT theory curve is predicted by fitting the measured $\xi_{\rm mm}$ on scales larger than 4 Mpc/h with the model $\xi_{\rm mm} = \mathcal{F}(P_{\rm mm}^{\rm 1-Loop}(k) + c_{\rm s}^2 k^2 P_{\rm lin}(k))$. We can see that EFT shows deviations at the 5% level, while *halofit* is a good description of $\xi_{\rm mm}$ over all scales and redshifts—typically within 2% for the bins with percent-level error bars on the measurement.

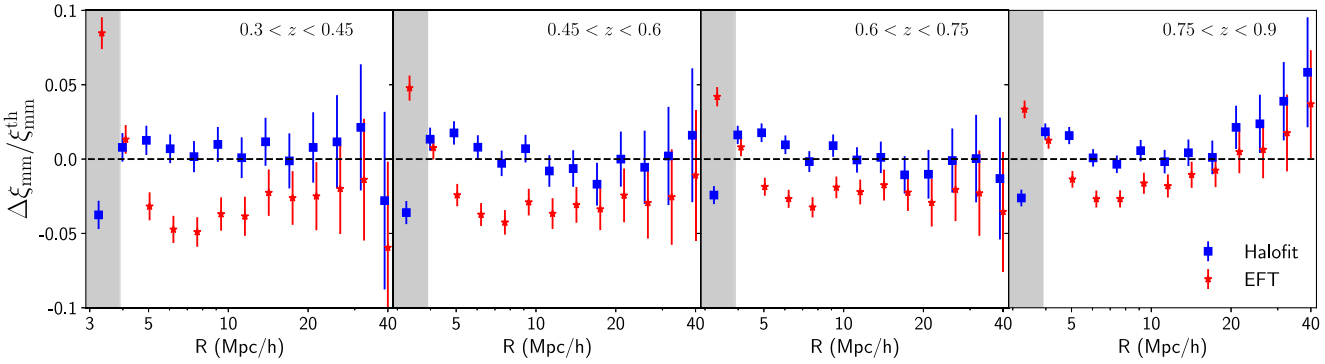

FIG. 2. Residuals of the matter-matter correlation function for the four tomographic bins (from left to right) when using *halofit* and EFT as the theoretical model. The difference between the model and measurements from the MICE simulations is plotted. *Halofit* performs significantly better on small scales. The reduced χ^2 for *halofit* using the data points above 4 Mpc/h (outside of the gray shaded regions) are 0.36, 0.53, 0.49, and 0.55 for the four tomographic bins. The red and blue points are staggered for clarity.

B. Goodness of fit

To assess the goodness of fit of the models, we use the reduced χ^2. For a good fit to n_d number of data points, using a model with n_v free parameters, we expect the $\chi^2/\text{d.o.f.}$ to have a mean of 1 and a standard deviation of $\sqrt{2/\text{d.o.f.}}$, where $\text{d.o.f.} = n_d - n_v$ is the total number of degrees of freedom.

C. FAST-PT

The mode coupling kernels that appear in perturbative terms, such as the higher-order bias contributions in Eq. (8), in Fourier space take the form of convolution integrals. For example, in standard perturbation theory, we expand the evolved overdensity field of tracers in terms of the linear overdensity, up to third order. This results in terms in the power spectrum that are proportional to $P_{22}(k)$ (given by the ensemble average $\langle\delta^{(2)}\delta^{(2)}\rangle$) and $P_{13}(k)$ (given by $\langle\delta^{(1)}\delta^{(3)}\rangle$). These kernels can be efficiently evaluated using fast Fourier transform techniques presented in Refs. [66–68], if one transforms these convolution integrals to the prescribed general form. We use the publicly available Python code FAST-PT as detailed in McEwen *et al.* [66] to evaluate all the PT kernels, which is also tested against a C version of the code, CFASTPT.[2]

D. Covariance estimation

We estimate a covariance for the data vector by applying the jackknife method [69,70] to the simulation split into N_{jk} number of patches. We use the k-means clustering algorithm to get the patches, which roughly divides the octant of sky occupied by our galaxy samples into N_{jk} equal-area patches. We use these same patches for covariance calculation in each of our tomographic bins. The accuracy of the estimated covariance increases with increasing N_{jk} and for scales much smaller than the size of an individual patch [71,72]. As the total area of the mock catalogs is fixed, changing the number of jackknife patches changes each patch's size.

In order to provide constraints on both nonlinear and linear bias parameters, the analysis requires a covariance estimate that correctly captures the auto- and correlations between radial bins over both small and large scales to provide constraints on both nonlinear and linear bias parameters. We find that we need to limit the analysis to $z > 0.3$ to achieve stable covariance estimates. For this reason, we do not analyze the MICE catalog over the first tomographic bin used in the DES-Y1 analysis ($0.15 < z < 0.3$).

We estimate the jackknife covariance using $N_{jk} = 300$ patches. For the lowest redshift bin ($0.3 < z < 0.45$), this results in an individual jackknife patch with a side length of approximately 100 Mpc/h. We determine the maximum scale included in our analysis by varying the number of patches and comparing the estimated errors at different scales. We find the covariance estimate to be stable below 40 Mpc/h and use this as our maximum scale cut. These tests are detailed in Appendix A.

We explicitly remove the cross covariance between tomographic bins, as there is negligible overlap in the galaxy samples of two different redshift bins, and as the length scales of interest are much smaller than the radial extent of the tomographic bins. We correct for biases in the inverse covariance (when calculating the reduced χ^2) due to the finite number of jackknife patches using the procedure described in Hartlap *et al.* [73].

Note that Fig. 11 shows the signal-to-noise ratio for these 3D statistics for each radial bin for our *fiducial* covariance.

V. RESULTS

A. Measurements

We split the galaxy sample into four tomographic bins, following the DES Year 1 analysis (DES Collaboration *et al.* [58]). The redshift ranges for the four bins are $0.3 < z < 0.45$, $0.45 < z < 0.6$, $0.6 < z < 0.75$, and $0.75 < z < 0.9$.

The auto- and cross-correlations measured with the galaxy and matter catalogs in the MICE simulations are shown in Fig. 3. We use the Landy-Szalay estimator [74] to estimate the correlation functions ξ_{gg}, ξ_{gm}, and ξ_{mm} for all the N_{jk} jackknife patches (see Sec. IV D). We create a random catalog with 10 times the number of galaxies in each tomographic bin and with number densities corresponding to a smoothed galaxy number density. We then use the ratios ξ_{gg}/ξ_{mm} and ξ_{gm}/ξ_{mm} to create our data-vector and jackknife covariance. We use the public code Treecorr [75] to measure the cross-correlations. We jointly fit these ratios ξ_{gg}/ξ_{mm} and ξ_{gm}/ξ_{mm} with PT models mentioned in Sec. IV A, as described next.

B. Results on fitting the 3D correlation functions

As a first analysis step, we fit the correlation function ratios measured from the simulation with the three models, A, B, and C [Eq. (23)], described in Sec. IV A. Model A only has one free parameter, linear bias b_1, while Model B and C in principle have b_1, b_2, b_s, b_{3nl}, and $b_{\nabla^2\delta}$ as free parameters. Here $b_{\nabla^2\delta}$ is the higher-derivative bias parameter. Among these parameters, by using the equivalence of Lagrangian and standard Eulerian perturbation theory (see Sec. II D), we can write b_s and b_{3nl} in terms of b_1 as their coevolution value. Therefore, the simplest complete one-loop model has b_1, b_2, and $b_{\nabla^2\delta}$ as free parameters. We fit our measurements while varying the number of free parameters in both Model B and Model C, to find the minimum number of parameters needed to describe the measured correlation function for different scale cuts.

[2]FAST-PT is available at https://github.com/JoeMcEwen/FAST-PT, and CFASTPT is available at https://github.com/xfangcosmo/cfastpt.

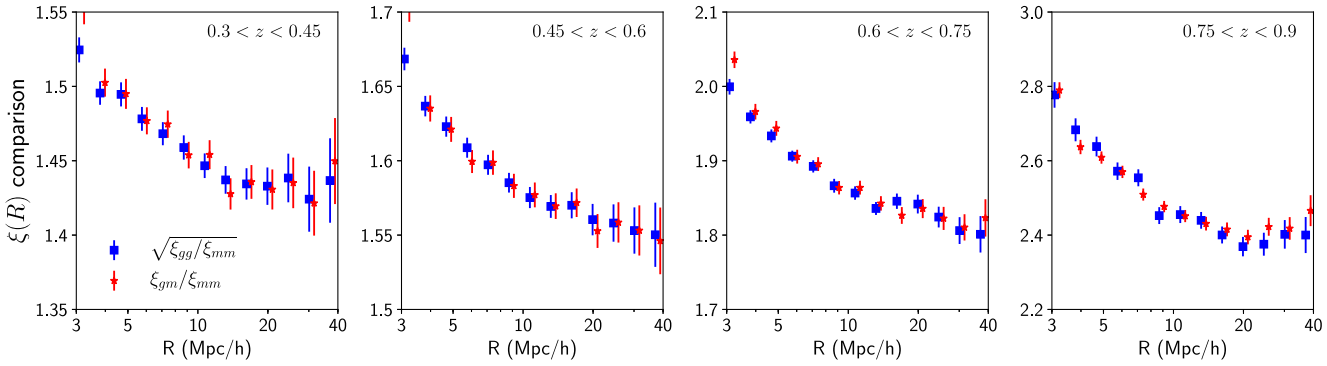

FIG. 3. Measurements of the ratio of the 3D galaxy-matter correlation functions (ξ_{gg}) and the matter-matter autocorrelation (ξ_{mm}) for the four tomographic bins of the redMaGiC galaxy sample in MICE simulations. The error bars are estimated from jackknife covariances. We fit PT models to the ratios ξ_{gg}/ξ_{mm} and ξ_{gm}/ξ_{mm}, as shown in subsequent figures.

We analyze the MICE data vector with two different minimum scale cuts: 8 Mpc/h and 4 Mpc/h. In Fig. 4, we compare the marginalized constraints on $b_{\nabla^2\delta}$ for Models B and C for each redshift bin. The marginalized constraints on $b_{\nabla^2\delta}$ are consistent with zero for Model C for all redshift bins and both scale cuts. In contrast, Model B shows significant detection of the $b_{\nabla^2\delta}$ term. It appears that the EFT term mostly captures the departure of the matter correlation function model from the truth.

Figure 5 compares the goodness of fit of different models by showing the reduced χ^2 estimated from the best fit of various model choices (as given in the x axis). We find that using Model C with only b_1 and b_2 as free parameters gives a reduced χ^2 consistent with 1 for all redshift bins (with b_s and b_{3nl} fixed to their coevolution value and $b_{\nabla^2\delta} = 0$).

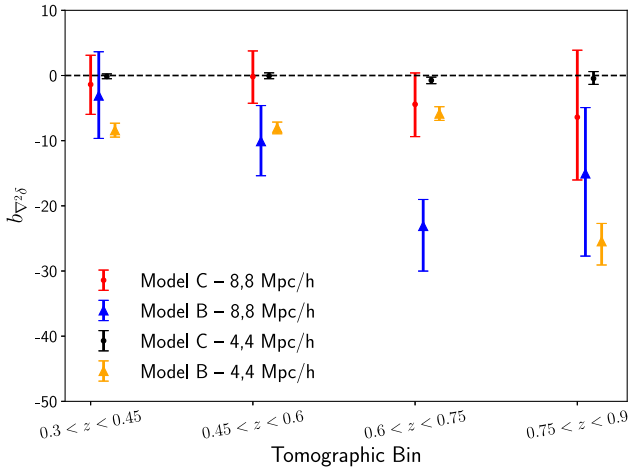

FIG. 4. The effective field theory parameter ($b_{\nabla^2\delta}$) estimated from two different models, described in Eq. (23), at two different scale cuts and using the redMaGiC galaxy sample. For example, the red points are the result of a joint analysis of ratios ξ_{gg}/ξ_{mm} and ξ_{gm}/ξ_{mm} (see Fig. 3) above 8 Mpc/h using Model C with free b_1, b_2, and $b_{\nabla^2\delta}$ parameters for each tomographic bin. We see that when the matter-matter correlation function is described by a nonlinear *halofit* (Model C), the marginalized EFT terms are consistent with zero for all redshifts and both scale cuts.

Hence, we conclude that adding these as free parameters is not needed to model the measurements on the scales considered here. In what follows, we consider this model choice of using one-loop PT with free b_1 and b_2 as our *fiducial* model. We also compare our fits to Model A, with free linear bias parameter b_1. The residuals of the observables—i.e., the ratios ξ_{gg}/ξ_{mm} and ξ_{gm}/ξ_{mm}—are shown in Fig. 6 for a scale cut of 8 Mpc/h, and in Fig. 7 for a scale cut of 4 Mpc/h. Note that *halofit* describes the matter-matter autocorrelation above scales of 4 Mpc/h at about the 2% level (see Fig. 2). In these and following figures, we refer to $\xi_{gg}^{\rm model} = \xi_{gg}/\xi_{mm}$ and $\xi_{gm}^{\rm model} = \xi_{gm}/\xi_{mm}$. Our *fiducial* model fits the simulations on scales above 4 Mpc/h and $z < 1$ within 2%, while the linear bias model performs significantly worse.

We also show the residuals of our fits to the Maglim sample in Fig. 7. We find that similar to the redMaGiC

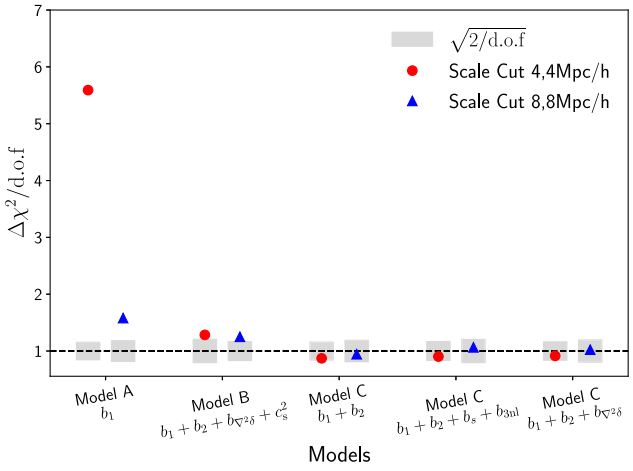

FIG. 5. The reduced χ^2 for various choices of free parameters in the models described in Eq. (23), when fitting the 3D measurements of the redMaGiC galaxy sample at scale cuts of 8 Mpc/h and 4 Mpc/h. The gray band denotes the expected error in the reduced χ^2 for a given number of degrees of freedom. We use Model C with two free parameters, b_1 and b_2 as our *fiducial* model (with b_s and b_{3nl} fixed to their coevolution value and $b_{\nabla^2\delta} = 0$).

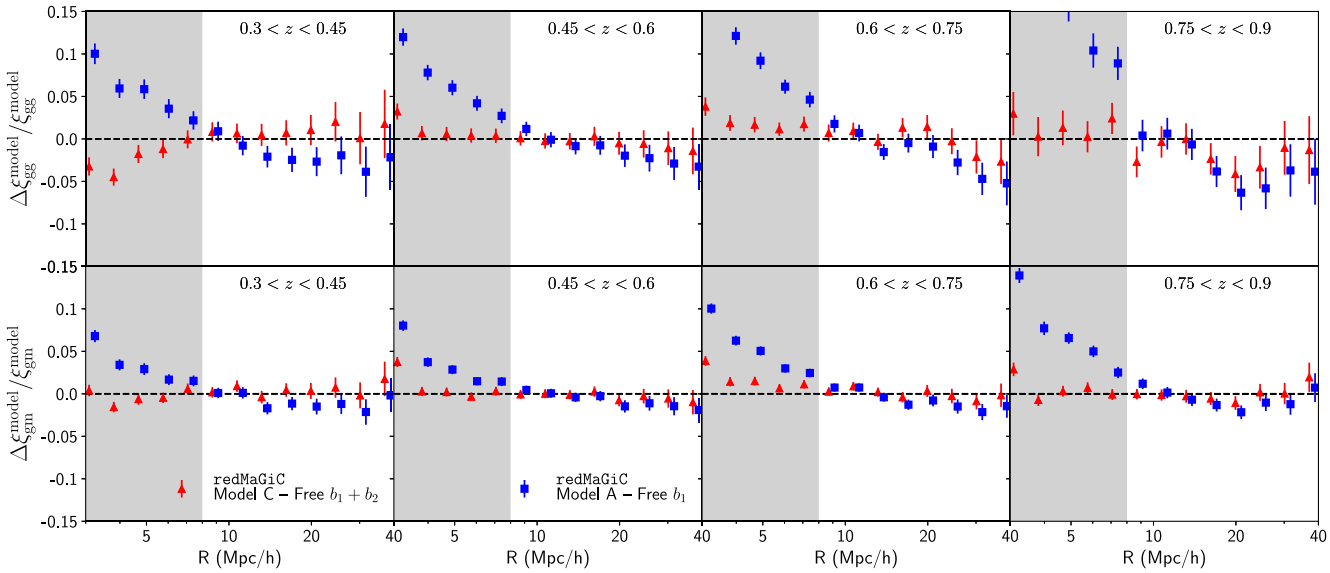

FIG. 6. Residuals [(data − best-fit)/best-fit] after performing a joint fit to the measurements of 3D statistics in the `redMaGiC` galaxy sample in the four tomographic bins shown in Fig. 3 with Model A (*linear bias model*) and our *fiducial* model, Model C (*one-loop PT* model, with free b_1 and b_2 bias parameters for each bin, and b_s and b_{3nl} fixed to the coevolution value, $b_{\nabla^2\delta} = 0$), and using *halofit* for matter-matter autocorrelation. Panels in the upper row show the residuals for the galaxy-galaxy correlation function, and panels in the lower row show the residuals for the galaxy-matter correlation function. Note that we refer to $\xi_{gg}^{model} = \xi_{gg}/\xi_{mm}$ and $\xi_{gm}^{model} = \xi_{gm}/\xi_{mm}$. Model C is an adequate description of the simulation measurements. We use a scale cut of 8 Mpc/h here and only fit the data points outside the gray region.

sample results, the *fiducial* model describes the measurements within about 2% above scales of 4 Mpc/h.

C. Relations between bias parameters

In this section, we revisit the approximation that the nonlinear bias parameters b_s and b_{3nl} follow the coevolution relation. The equivalence of the local Lagrangian and nonlocal Eulerian description predicts $b_s = -4/7(b_1 - 1)$ and $b_{3nl} = (b_1 - 1)$ (see Sec. II D). We test this assumption by freeing up these parameters, in addition to b_1 and b_2, and refitting the measurements with these extended models. Figure 8 shows the relation between the nonlinear bias parameters and b_1 at the two scale cuts and for both `redMaGiC` and `Maglim` galaxy samples. The points in each panel for each scale cut correspond to the four tomographic bins. The top panel shows the relation between b_1 and b_2 (when the parameters b_s and b_{3nl} are fixed to their coevolution values), the middle panel shows

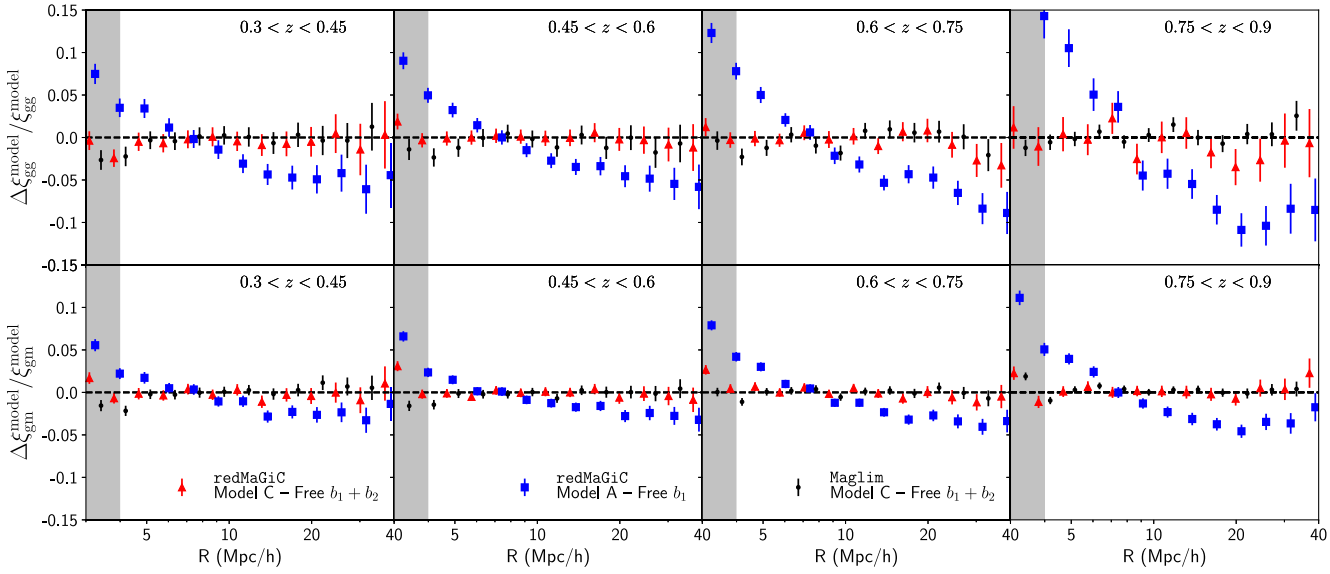

FIG. 7. Same as Fig. 6, but analyzed with a scale cut of 4 Mpc/h. Here we also show the residuals for the `Maglim` galaxy sample. Model C fits the simulation measurements with these smaller scale cuts for both `redMaGiC` and `Maglim` samples.

the relation between b_1 and b_s (when b_{3nl} is fixed to its coevolution value), and the bottom panel shows the relation between b_1 and b_{3nl} (when b_s is fixed to its coevolution value). The fits obtained when all the parameters are free have a larger uncertainty but are consistent with the other approaches: the relations between the parameters b_s-b_1 and b_{3nl}-b_1 are consistent with the expected coevolution value. We also note that the recovered relation with b_1 is consistent for the two scale cuts, which is a further test that the one-loop PT is a sufficient and complete model for the scales of interest in this analysis.

It is possible to predict the relation between b_2 and b_1 for our galaxy samples (the measurements are shown in the top panel of Fig. 8). However, unlike the b_s-b_1 and b_{3nl}-$b1$ relations, predicting the b_2-b_1 relation requires knowledge of the HOD of galaxy samples. Since an accurate HOD of the galaxy sample in data is challenging and not yet available for DES, we have treated b_2 as a free parameter. Therefore, only the measurements of the b_2-b_1 relation from simulations are shown in Fig. 8.

D. Inferences for the projected statistics

As described in Sec. II E, we can convert our measurements and fits for the 3D correlation functions to the projected statistics typically used by the imaging surveys. We show such a conversion in Fig. 9 for galaxy number densities in MICE simulations corresponding to the redMaGiC galaxies satisfying $0.3 < z_l < 0.45$ and the fourth source tomographic bin as used in the DES Y1 analysis. Note that Fig. 9 does not show direct measurements of $w(\theta)$ and γ_t, but a transformation of the measured and best-fit data vector to angular statistics. Since our analysis is based on the ratios ξ_{gg}/ξ_{mm} and ξ_{gm}/ξ_{mm}, we first convert our measured data vector and best-fit theory curves to ξ_{gg} and ξ_{gm} and then apply Eqs. (11) and (22) to estimate angular correlation functions. We use the *halofit* prediction of ξ_{mm}, which is a good fit to the matter-matter autocorrelation for our scales of interest (see Fig. 2) to convert the ratios to ξ_{gg} and ξ_{gm}.

The error bars in Fig. 9 are calculated from Gaussian covariance,[3] as we do not expect significant non-Gaussian contribution to the covariance of the angular statistics (see Ref. [77]). The covariance is estimated using all the galaxies satisfying the redshift criteria mentioned above in the MICE simulation. Explicitly, we generate this covariance with lens and source galaxies covering 5156.6 square degrees with number densities (per square arc-minutes) of lens galaxies in four tomographic bins corresponding to 0.039, 0.058, 0.045, and 0.028, respectively. The number density and shape noise of source galaxies are assumed to be the same as in DES Y3 [78]. Due to a similar area and number densities, this

[3]We use the COSMOSIS package [76] https://bitbucket.org/joezuntz/cosmosis/wiki/Home.

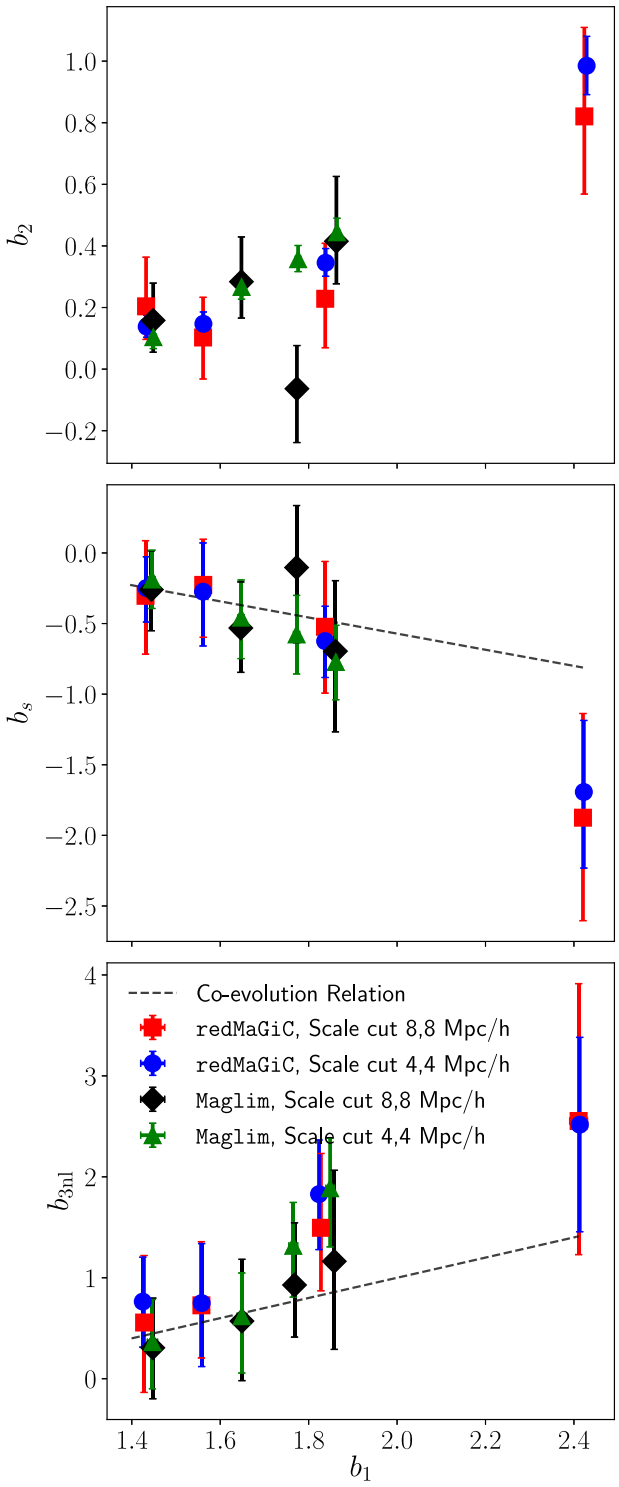

FIG. 8. The relation between the best-fit nonlinear bias parameters and the linear bias parameter b_1 for the four tomographic bins at two different scale cuts. We show the results for both redMaGiC and Maglim galaxy samples. The top panel shows the second-order bias parameter b_2, with b_s and b_{3nl} fixed to their coevolution Lagrangian values. The middle panel shows b_s (with b_{3nl} fixed to the coevolution Lagrangian value). The bottom panel shows b_{3nl} (with b_s fixed to the coevolution Lagrangian value).

covariance is comparable to the expected DES Year 3 covariance [78]. Note that the shaded region corresponds to scales below 4 Mpc/h, which are not used in the 3D fits. The top panel shows the projected galaxy correlation function $w(\theta)$, and the bottom panel shows the galaxy-galaxy lensing signal $\gamma_t(\theta)$. Note that in order to estimate γ_t, we fit for the point-mass term as described in Sec. II E. This best-fit value of the point-mass term is obtained by fitting for the coefficient B in Eq. (22).

Figure 9 demonstrates that our model describes the projected angular correlation functions well above scales

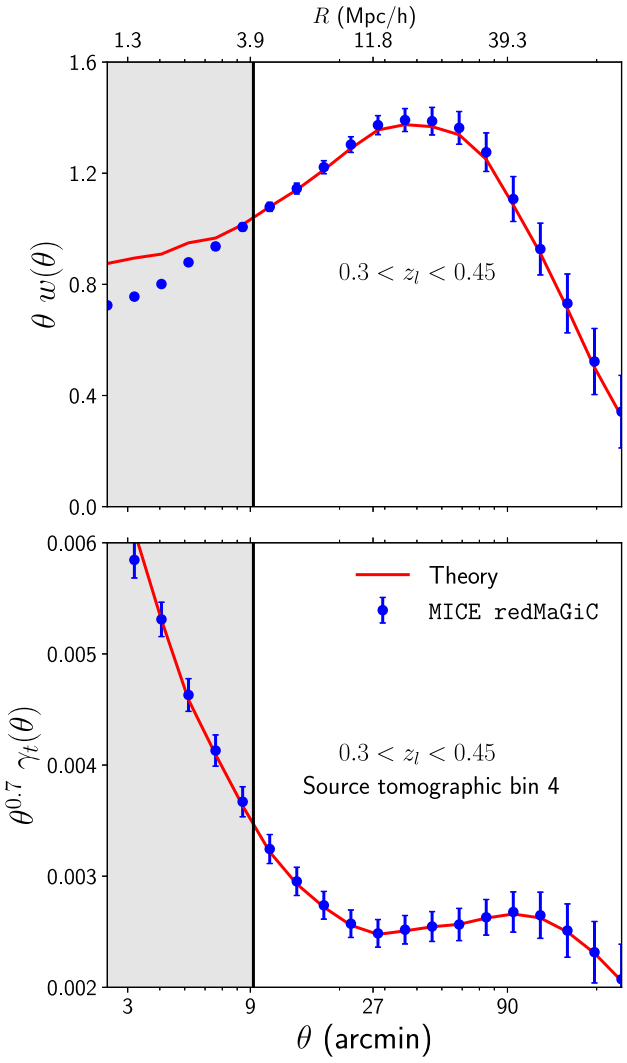

FIG. 9. The blue error bars show the projected statistics $w(\theta)$ and $\gamma_t(\theta)$ transformed from 3D measurements of `MICE redMaGiC` samples [using Eqs. (11) and (22)]. The red theory curve is also estimated similarly from the best fit to the 3D statistics on scales above 4 Mpc/h (see Fig. 7). These transformations use the $n(z)$ corresponding to our first lens tomographic bin ($0.3 < z_l < 0.45$) (of the `redMaGiC` sample) and the fourth source redshift bin (see Ref. [59]) in the `MICE` simulation. The shaded region shows the scale cut of 4 Mpc/h. The error bars are estimated using the Gaussian halo model covariance for the best-fit bias values. The theory curve for γ_t includes the contribution from the point mass [see Eq. (22)].

of 4 Mpc/h. The error bars in that figure provide a DES-Y3-like benchmark for such an agreement. Note that the fractional statistical uncertainties for projected statistics are much larger than their 3D counterparts. Hence, the 3D tests presented in Sec. V B are substantially more stringent than the projected statistics require.

The analysis of measured $w(\theta)$ and $\gamma_t(\theta)$ is detailed in Appendix C.

E. Comparison with other studies in literature

There have been multiple studies in the literature probing the validity of PT models using simulations [31–35]. Most of these studies have focused on Fourier space rather than configuration space. One reason for this choice is that nonlinear and linear scales are better separated in Fourier space, while in configuration space, even large scales receive a contribution from nonlinear Fourier modes. However, many cosmic surveys perform their cosmological parameter analysis in configuration space, as it is easier to take into account a noncontiguous mask and depth variations. Hence, an understanding of the validity of PT models is required in real space to get unbiased cosmology constraints.

The Fourier space studies conducted by Saito *et al.* [31] and Angulo *et al.* [32] focus only on dark-matter halos and do not aim to reduce the number of free parameters required to explain the auto- and cross-correlations between dark matter halos and dark matter particles. Bella *et al.* [33] and Werner and Porciani [34] probe this question on the minimum number of bias parameters but again focus on dark matter halos as the biased tracers. Recently Eggemeier *et al.* [35] have conducted a study similar to ours in Fourier space using three different galaxy samples (mock SDSS and BOSS catalogs) and four halo samples. For a most general case, they find that a four-parameter model (linear, quadratic, cubic nonlocal bias, and constant shot noise with fixed quadratic tidal bias) can describe correlations between galaxies and matter catalogs, with the inclusion of scale-dependent noise from halo exclusion being particularly beneficial for the combination of auto- and cross-spectra. They also explore the restriction to a two-parameter model by imposing coevolution relations, as done in this paper, and find that in general, this reduces the highest Fourier mode for which the model is robust, but it can result in higher constraining power compared to the five-parameter model. However, this particular scenario is not general across samples and requires careful validation with simulations, as done here. The main differences in our study are that we work in configuration space with two different galaxy samples that have a higher number density, cover a wider redshift range, and probe smaller host halo masses. Our galaxy samples also have a significantly larger satellite fraction (for example, the first two `redMaGiC` bins have a ∼50% satellite fraction) compared to SDSS and BOSS catalogs.

These crucial differences make our study complementary to the above studies. Ours is especially relevant for imaging

surveys, as it is tailored to DES. The consistency of our conclusions with Eggemeier *et al.* [35] suggests that a two-parameter model may have wide applicability, particularly for surveys with different galaxy selections. This would be an extremely useful result and is worth investigating in detail for the next generation of surveys.

VI. CONCLUSION

We have presented an analysis of galaxy bias comparing perturbation theory and 3D correlation functions measured from N-body simulation-based mock catalogs. We used an effective PT model to analyze the galaxy-galaxy and galaxy-matter correlations jointly.

Our *fiducial* model successfully describes the measurements from simulations above a scale of 4 Mpc$/h$, which is significantly lower than the scale cut used in the DES Year 1 analysis (where a linear bias model was used). In addition to the linear bias parameter b_1, we include four bias parameters in our model: b_2, $b_{\rm s}$, $b_{\rm 3nl}$, and $b_{\nabla^2\delta}$. We find that treating only the first- and second-order bias parameters b_1 and b_2 as free parameters is sufficient to describe the correlation functions over the scales of interest. We find that the constraints on the higher-derivative bias parameter $b_{\nabla^2\delta}$ are consistent with zero in Model C, and we thus fix it to zero in our *fiducial* model. We demonstrate that fixing the parameters $b_{\rm s}$ and $b_{\rm 3nl}$ to their coevolution value maintains the accuracy of our model. The agreement of our model with measurements from simulations is typically at the 2% level over scales of interest. This is within the statistical uncertainty of our simulation measurements and below the requirements of the DES Year 3 analysis.

We show the relationship between the nonlinear and linear bias parameters at different redshifts and scale cuts. We find that the relationship between $b_{\rm s}$-b_1 and $b_{\rm 3nl}$-b_1 is consistent with the expectations from the coevolution relationship. Moreover, we find that the relationship between b_2-b_1 is consistent at different scale cuts, which is a useful validation of our model.

We have validated our model with two lens galaxy samples having different and broad host halo mass distribution—the `redMaGiC` and `Maglim` samples—that could be used in DES Y3 cosmological analyses, which combine the projected galaxy clustering signal, $w(\theta)$, and the galaxy-galaxy lensing signal, $\gamma_{\rm t}$. Note that these projected statistics have significantly higher (fractional) cosmic variance than their 3D counterparts, $\xi_{\rm gg}$ and $\xi_{\rm gm}$, due to the smaller number of independent modes. Furthermore, the statistical uncertainty of $\gamma_{\rm t}$ includes weak lensing shape noise, which is not included in the error budget of its 3D counterpart ($\xi_{\rm gm}$). Hence, we analyze 3D correlation functions, as the measurements from simulations are more precise and provide a percent-level test of our model.

The scales of interest (above 4 Mpc$/h$) are well above the one-halo regime, where differences in HOD implementations are greatest. So we expect that our conclusions about bias modeling with PT will have broad validity for the lensing and galaxy clustering analysis from imaging surveys. Nevertheless, at the percent level of accuracy, tests with a variety of schemes for assigning galaxies will be valuable. Moreover, pushing the analysis to higher redshift, or a completely different galaxy selection requires additional testing. We leave these studies for future work.

ACKNOWLEDGMENTS

We thank Ravi Sheth for valuable discussions regarding nonlinear bias models and the formalism of the paper. S. P. and B. J. are supported in part by U.S. Department of Energy Grant No. DE-SC0007901. E. K. is supported by U.S. Department of Energy Grant No. DE-SC0020247. Funding for the DES Projects has been provided by the U.S. Department of Energy, the U.S. National Science Foundation, the Ministry of Science and Education of Spain, the Science and Technology Facilities Council of the United Kingdom, the Higher Education Funding Council for England, the National Center for Supercomputing Applications at the University of Illinois at Urbana-Champaign, the Kavli Institute of Cosmological Physics at the University of Chicago, the Center for Cosmology and Astro-Particle Physics at the Ohio State University, the Mitchell Institute for Fundamental Physics and Astronomy at Texas A&M University, Financiadora de Estudos e Projetos, Fundação Carlos Chagas Filho de Amparo à Pesquisa do Estado do Rio de Janeiro, Conselho Nacional de Desenvolvimento Científico e Tecnológico and the Ministério da Ciência, Tecnologia e Inovação, the Deutsche Forschungsgemeinschaft, and the Collaborating Institutions in the Dark Energy Survey. The Collaborating Institutions are Argonne National Laboratory, the University of California at Santa Cruz, the University of Cambridge, Centro de Investigaciones Energéticas, Medioambientales y Tecnológicas-Madrid, the University of Chicago, University College London, the DES-Brazil Consortium, the University of Edinburgh, the Eidgenössische Technische Hochschule (ETH) Zürich, Fermi National Accelerator Laboratory, the University of Illinois at Urbana-Champaign, the Institut de Ciències de l'Espai (IEEC/CSIC), the Institut de Física d'Altes Energies, Lawrence Berkeley National Laboratory, the Ludwig-Maximilians Universität München and the associated Excellence Cluster Universe, the University of Michigan, the National Optical Astronomy Observatory, the University of Nottingham, The Ohio State University, the University of Pennsylvania, the University of Portsmouth, SLAC National Accelerator Laboratory, Stanford University, the University of Sussex, Texas A&M University, and the OzDES Membership Consortium. Based in part on observations at Cerro Tololo Inter-American Observatory, National Optical Astronomy Observatory, which is operated by the Association of Universities for Research in Astronomy

(AURA) under a cooperative agreement with the National Science Foundation. The DES data management system is supported by the National Science Foundation under Grants No. AST-1138766 and No. AST-1536171. The DES participants from Spanish institutions are partially supported by MINECO under Grants No. AYA2015-71825, No. ESP2015-66861, No. FPA2015-68048, No. SEV-2016-0588, No. SEV-2016-0597, and No. MDM-2015-0509, some of which include ERDF funds from the European Union. I. F. A. E. is partially funded by the CERCA program of the Generalitat de Catalunya. Research leading to these results has received funding from the European Research Council under the European Union's Seventh Framework Program (FP7/2007-2013) including ERC Grant Agreements No. 240672, No. 291329, and No. 306478. We acknowledge support from the Brazilian Instituto Nacional de Ciência e Tecnologia (INCT) e-Universe (CNPq Grant No. 465376/2014-2). This manuscript has been authored by Fermi Research Alliance, LLC, under Contract No. DE-AC02-07CH11359 with the U.S. Department of Energy, Office of Science, Office of High Energy Physics. The United States Government retains, and the publisher, by accepting the article for publication, acknowledges that the United States Government retains, a nonexclusive, paid-up, irrevocable, worldwide license to publish or reproduce the published form of this manuscript, or allow others to do so, for United States Government purposes.

APPENDIX A: COVARIANCE OF THE DATA VECTORS

The measurements of the correlation functions ξ_{gg} and ξ_{gm} are highly correlated in the configuration space due to the mixing of modes. However, since the correlation function ξ_{mm} is also impacted by similar mode-mixing, analyzing the ratio of the correlation functions ξ_{gg}/ξ_{mm} and ξ_{gm}/ξ_{mm} makes the covariance more diagonal. In Fig. 10, we compare the correlation matrix for ξ_{gg} and ξ_{gg}/ξ_{mm} for the third tomographic bin for 20 radial bins ranging from 0.8 to 50 Mpc/h. We clearly see that analyzing the ratio gives us a much better-behaved correlation matrix.

We generate the *fiducial* jackknife covariance from 300 patches distributed over the simulation footprint. As the total area populated by both our galaxy sample is equal to one octant of the sky, changing the number of jackknife patches changes the size of each patch. In Fig. 11, we compare the signal-to-noise estimate when using a different number of patches. We see that the diagonal elements of the covariance are robust to changes in the number of patches. We have also compared the changes in best-fit curves when using the covariance matrix generated using a different

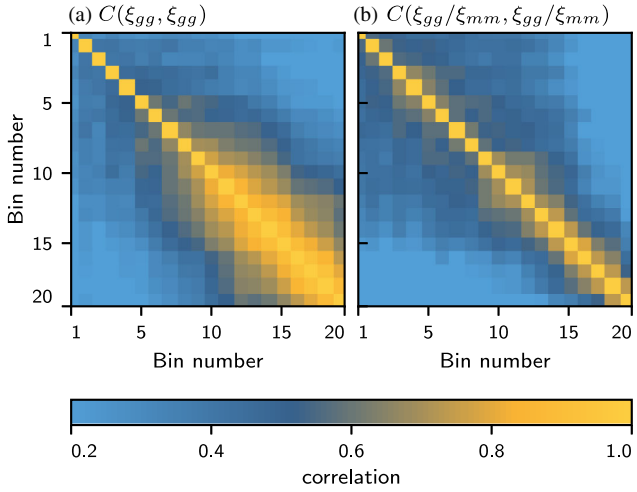

FIG. 10. The correlation matrix for the two-point galaxy correlation function ξ_{gg} and the ratio ξ_{gg}/ξ_{mm} for the second tomographic bin. Both correlation matrices are estimated using 300 jackknife patches. We see that the covariance is more diagonal for the ratio.

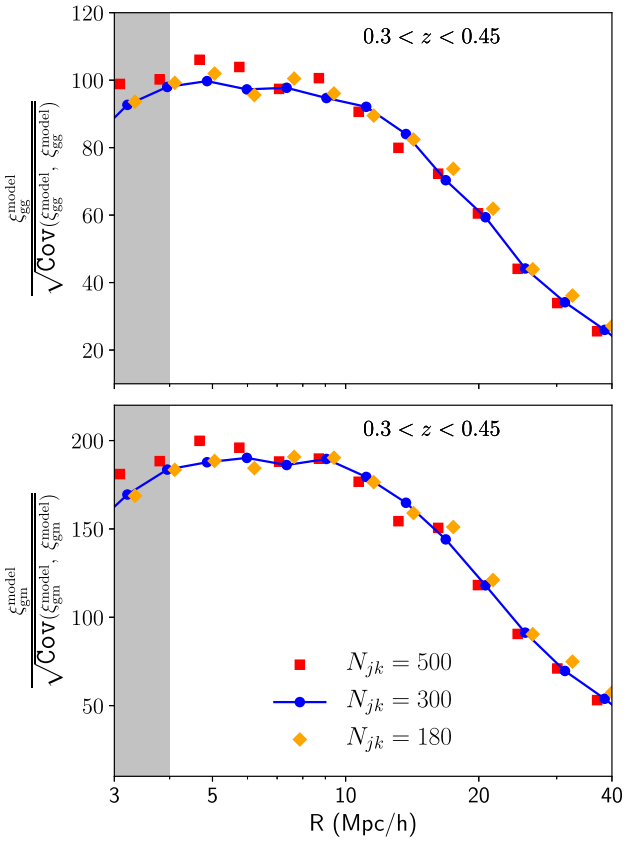

FIG. 11. The comparison of error bars (and signal-to-noise ratios) estimated using the jackknife procedure, for a different number of patches. We show the comparison for the smallest tomographic bin used in our analysis, since that is most susceptible to the sizes of the jackknife patches. Also, since the covariance matrix of the correlation function ratios has small cross-bin covariance (see Fig. 10), we only compare the diagonal value. The blue points (and solid curve) correspond to our *fiducial* choice of 300 as the number of jackknife patches used for covariance estimation.

number of patches. We get consistent reduced χ^2 and best-fit curves for $z > 0.3$. However, we find that we cannot get a robust covariance for the tomographic bin corresponding to $z < 0.3$ without sacrificing large-scale information (which is required to constrain the linear bias parameter). For this reason, we only analyze the tomographic bins satisfying $z > 0.3$ and find that with 300 patches, we can get a robust estimate of jackknife covariance.

APPENDIX B: RESULTS WITH FITTING ξ_{gg} AND ξ_{gm} DIRECTLY

As mentioned in the main text, we consider the ratios ξ_{gg}/ξ_{mm} and ξ_{gm}/ξ_{mm} as our data vector. This ratio is more sensitive to the galaxy-matter connection than the correlation functions ξ_{gg} and ξ_{gm} themselves. However, when we try to fit directly the correlation functions, ξ_{gg} and ξ_{gm}, our conclusions do not change. The residuals of ξ_{gg} and ξ_{gm} using our *fiducial* model are shown in Fig. 12 for the third tomographic bin. We compare the residuals obtained when directly fitting the correlation functions ξ_{gg}, ξ_{gm} with the results shown in the main text obtained when fitting the ratios of the correlation functions, ξ_{gg}/ξ_{mm}, ξ_{gm}/ξ_{mm}. We find that our residuals are consistent with zero above the scales of 4 Mpc$/h$ for both data vectors.

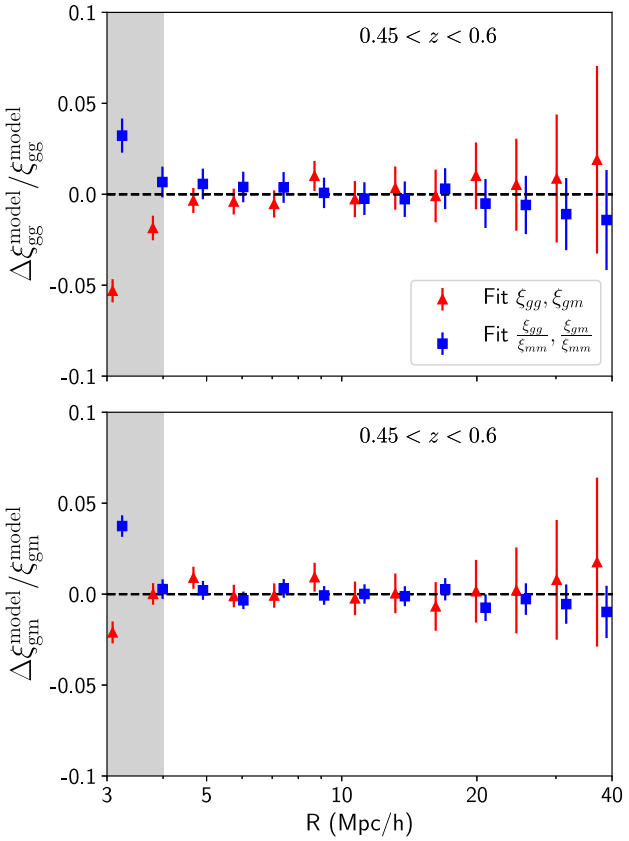

FIG. 12. Comparing the residuals when fitting the measured correlation functions ξ_{gg}, ξ_{gm} directly and when fitting the ratio ξ_{gg}/ξ_{mm}, ξ_{gm}/ξ_{mm} for the second tomographic bin. We use our *fiducial* model as our theory model in both cases. We find the fits are consistent.

APPENDIX C: ANALYZING THE 2D CORRELATION FUNCTION AT FIXED COSMOLOGY

As described in the Sec. II E and Fig. 9, we convert the 3D statistics to the projected statistics. However, we can also fit our perturbation theory models directly to the measured projected statistics. Therefore, in this Appendix, we fit our *fiducial* model to the projected statistics $w(\theta)$ and γ_t in the four lens and source tomographic bins. We refer the readers to MacCrann *et al.* [59] for the details about the estimation of the projected statistics and the tomographic redshift distribution of our bins.

The residuals of this model are shown in Fig. 13 when using scales above 4 Mpc$/h$. For the observable γ_t, we show the results for only the fourth source bin and all four lens tomographic bins (since this has the highest signal-to-noise ratio). The fit has a reduced χ^2 of 0.88. There are some points in the residuals that are inconsistent with zero; however, as there is a significant correlation between different radial bins, they do not impact the χ^2 of the fit. The measured relation between b_2 and b_1 from this model is shown in Fig. 14. We also compare this relationship with the one inferred from the 3D measurements and find them consistent.

Hence, when fitting the measured projected correlation functions directly, we also get a reduced χ^2 consistent with one. These results motivate us to model the correlations on the scales down to 4 Mpc$/h$ in the DES Y3 cosmological analysis. To determine the scale cuts for DES analysis with a nonlinear bias model, we will study the cosmological parameter biases in a future study with the range of scale cut choices motivated by this study.

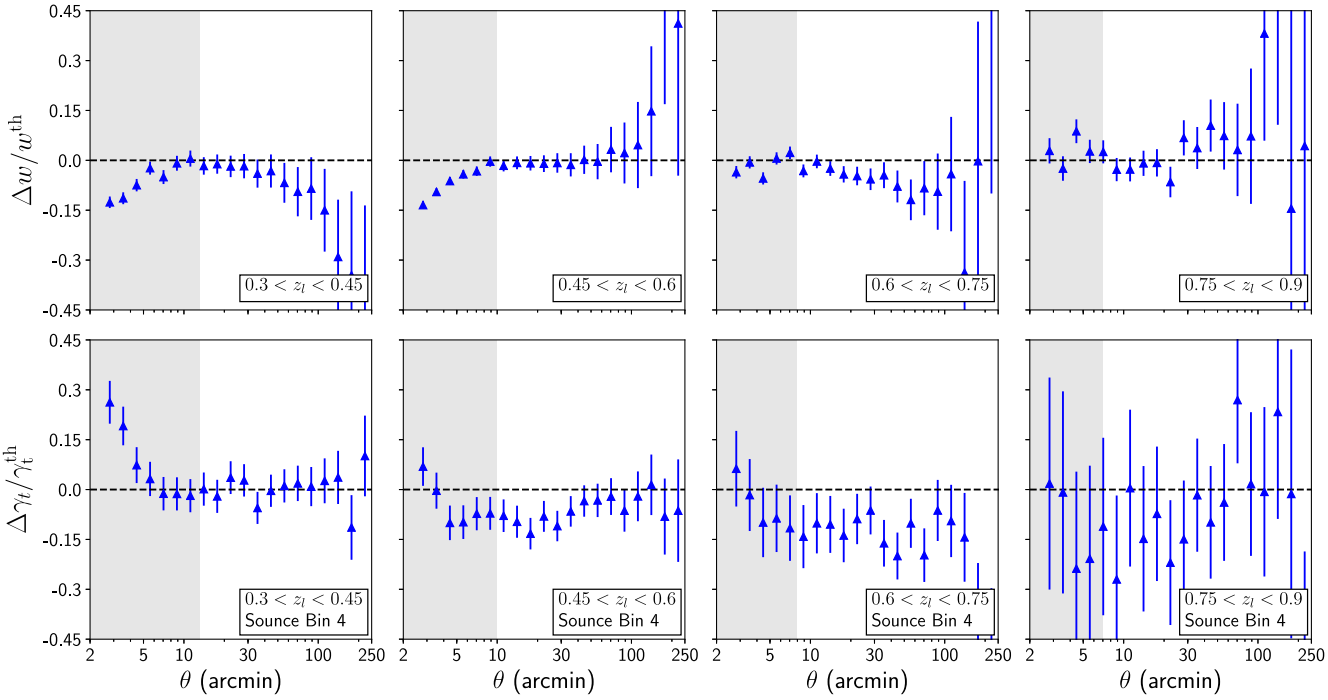

FIG. 13. Residual from joint fits to the measurements of the 2D statistics, in four tomographic lens and source bins [see Ref. [59] for source $n(z)$], using our *fiducial* model. The top row shows the residuals for $w(\theta)$, and the bottom row for γ_t, with the source redshift distribution taken as the fourth bin in the DES Y1 analysis. We use a scale cut of 4 Mpc$/h$ here and only fit the data points outside the gray region. The reduced χ^2 including all the data points (total degrees of freedom $= 342$) above the scale cut is 0.88.

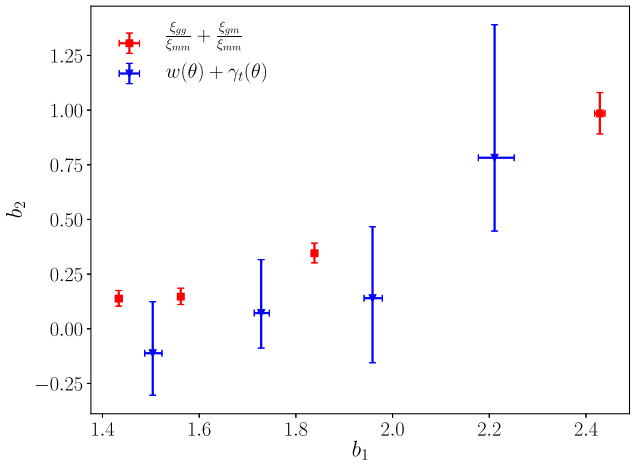

FIG. 14. The relation between the marginalized nonlinear and linear bias parameters for four tomographic bins estimated from fitting $w(\theta)$ and γ_t. We also compare these values to the ones estimated from the 3D correlation functions and find a consistent b_2-b_1 relation.

[1] F. Bernardeau, S. Colombi, E. Gaztanaga, and R. Scoccimarro, Phys. Rep. **367**, 1 (2002).
[2] V. Desjacques, D. Jeong, and F. Schmidt, Phys. Rep. **733**, 1 (2018).
[3] B. Jain and E. Bertschinger, Astrophys. J. **431**, 495 (1994).
[4] M. H. Goroff, B. Grinstein, S. J. Rey, and M. B. Wise, Astrophys. J. **311**, 6 (1986).

[5] F. R. Bouchet, S. Colombi, E. Hivon, and R. Juszkiewicz, Astron. Astrophys. **296**, 575 (1995), https://ui.adsabs.harvard.edu/abs/1995A%26A...296..575B/abstract.
[6] T. Matsubara, Phys. Rev. D **77**, 063530 (2008).
[7] M. Crocce and R. Scoccimarro, Phys. Rev. D **73**, 063519 (2006).
[8] J. J. M. Carrasco, M. P. Hertzberg, and L. Senatore, J. High Energy Phys. 09 (2012) 082.
[9] Z. Vlah, M. White, and A. Aviles, J. Cosmol. Astropart. Phys. 09 (2015) 014.
[10] A. Perko, L. Senatore, E. Jennings, and R. H. Wechsler, arXiv:1610.09321.
[11] J. N. Fry and E. Gaztanaga, Astrophys. J. **413**, 447 (1993).
[12] P. Coles, Mon. Not. R. Astron. Soc. **262**, 1065 (1993).
[13] A. F. Heavens, S. Matarrese, and L. Verde, Mon. Not. R. Astron. Soc. **301**, 797 (1998).
[14] R. J. Scherrer and D. H. Weinberg, Astrophys. J. **504**, 607 (1998).
[15] P. McDonald and A. Roy, J. Cosmol. Astropart. Phys. 08 (2009) 020.
[16] T. Matsubara, Phys. Rev. D **90**, 043537 (2014).
[17] J. Carlson, B. Reid, and M. White, Mon. Not. R. Astron. Soc. **429**, 1674 (2013).
[18] C. Blake, S. Brough, M. Colless, C. Contreras, W. Couch, S. Croom, T. Davis, M. J. Drinkwater, K. Forster, D. Gilbank *et al.*, Mon. Not. R. Astron. Soc. **415**, 2876 (2011).
[19] F. A. Marín, C. Blake, G. B. Poole, C. K. McBride, S. Brough, M. Colless, C. Contreras, W. Couch, D. J. Croton, S. Croom *et al.*, Mon. Not. R. Astron. Soc. **432**, 2654 (2013).
[20] A. G. Sánchez, R. Scoccimarro, M. Crocce, J. N. Grieb, S. Salazar-Albornoz, C. D. Vecchia, M. Lippich, F. Beutler, J. R. Brownstein, C.-H. Chuang *et al.*, Mon. Not. R. Astron. Soc. **464**, 1640 (2017).
[21] H. Gil-Marín, W. J. Percival, L. Verde, J. R. Brownstein, C.-H. Chuang, F.-S. Kitaura, S. A. Rodríguez-Torres, and M. D. Olmstead, Mon. Not. R. Astron. Soc. **465**, 1757 (2017).
[22] F. Beutler, H.-J. Seo, S. Saito, C.-H. Chuang, A. J. Cuesta, D. J. Eisenstein, H. Gil-Marín, J. N. Grieb, N. Hand, F.-S. Kitaura *et al.*, Mon. Not. R. Astron. Soc. **466**, 2242 (2017).
[23] J. N. Grieb, A. G. Sánchez, S. Salazar-Albornoz, R. Scoccimarro, M. Crocce, C. Dalla Vecchia, F. Montesano, H. Gil-Marín, A. J. Ross, F. Beutler *et al.*, Mon. Not. R. Astron. Soc. **467**, stw3384 (2017).
[24] G. D'Amico, J. Gleyzes, N. Kokron, D. Markovic, L. Senatore, P. Zhang, F. Beutler, and H. Gil-Marín, J. Cosmol. Astropart. Phys. 05 (2020) 005.
[25] M. M. Ivanov, M. Simonović, and M. Zaldarriaga, Phys. Rev. D **101**, 083504 (2020).
[26] A. Cooray and R. Sheth, Phys. Rep. **372**, 1 (2002).
[27] A. A. Berlind and D. H. Weinberg, Astrophys. J. **575**, 587 (2002).
[28] Z. Zheng, A. A. Berlind, D. H. Weinberg, A. J. Benson, C. M. Baugh, S. Cole, R. Davé, C. S. Frenk, N. Katz, and C. G. Lacey, Astrophys. J. **633**, 791 (2005).
[29] J. Clampitt, C. Sánchez, J. Kwan, E. Krause, N. MacCrann, Y. Park, M. A. Troxel, B. Jain, E. Rozo, E. S. Rykoff *et al.*, Mon. Not. R. Astron. Soc. **465**, 4204 (2017).
[30] I. Zehavi *et al.* (SDSS Collaboration), Astrophys. J. **630**, 1 (2005).
[31] S. Saito, T. Baldauf, Z. Vlah, U. Seljak, T. Okumura, and P. McDonald, Phys. Rev. D **90**, 123522 (2014).
[32] R. Angulo, M. Fasiello, L. Senatore, and Z. Vlah, J. Cosmol. Astropart. Phys. 09 (2015) 029.
[33] L. F. de la Bella, D. Regan, D. Seery, and D. Parkinson, J. Cosmol. Astropart. Phys. 07 (**2020**) 011.
[34] K. F. Werner and C. Porciani, Mon. Not. R. Astron. Soc. **492**, 1614 (2020).
[35] A. Eggemeier, R. Scoccimarro, M. Crocce, A. Pezzotta, and A. G. Sánchez, Phys. Rev. D **102**, 103530 (2020).
[36] T. Matsubara, Astrophys. J. **525**, 543 (1999).
[37] A. Dekel and O. Lahav, Astrophys. J. **520**, 24 (1999).
[38] A. Taruya and J. Soda, Astrophys. J. **522**, 46 (1999).
[39] A. Eggemeier, R. Scoccimarro, and R. E. Smith, Phys. Rev. D **99**, 123514 (2019).
[40] K. C. Chan, R. Scoccimarro, and R. K. Sheth, Phys. Rev. D **85**, 083509 (2012).
[41] J. N. Fry, Astrophys. J. Lett. **461**, L65 (1996).
[42] T. Baldauf, U. C. V. Seljak, V. Desjacques, and P. McDonald, Phys. Rev. D **86**, 083540 (2012).
[43] C. Modi, E. Castorina, and U. Seljak, Mon. Not. R. Astron. Soc. **472**, 3959 (2017).
[44] F. C. van den Bosch, S. More, M. Cacciato, H. Mo, and X. Yang, Mon. Not. R. Astron. Soc. **430**, 725 (2013).
[45] N. MacCrann, J. Blazek, B. Jain, and E. Krause, Mon. Not. R. Astron. Soc. **491**, 5498 (2020).
[46] T. Baldauf, R. E. Smith, U. Seljak, and R. Mandelbaum, Phys. Rev. D **81**, 063531 (2010).
[47] B. Flaugher, H. T. Diehl, K. Honscheid, T. M. C. Abbott, O. Alvarez, R. Angstadt, J. T. Annis, M. Antonik, O. Ballester, L. Beaufore *et al.*, Astron. J. **150**, 150 (2015).
[48] I. Sevilla *et al.*, arXiv:1109.6741.
[49] E. Morganson *et al.* (DES Collaboration), Publ. Astron. Soc. Pac. **130**, 074501 (2018).
[50] N. Sevilla *et al.* (to be published).
[51] E. Sheldon *et al.* (to be published).
[52] V. Springel, Mon. Not. R. Astron. Soc. **364**, 1105 (2005).
[53] P. Fosalba, M. Crocce, E. Gaztañaga, and F. J. Castander, Mon. Not. R. Astron. Soc. **448**, 2987 (2015).
[54] J. Carretero, F. J. Castander, E. Gaztañaga, M. Crocce, and P. Fosalba, Mon. Not. R. Astron. Soc. **447**, 646 (2015).
[55] M. Crocce, F. J. Castander, E. Gaztañaga, P. Fosalba, and J. Carretero, Mon. Not. R. Astron. Soc. **453**, 1513 (2015).
[56] E. Rozo, E. S. Rykoff, A. Abate, C. Bonnett, M. Crocce, C. Davis, B. Hoyle, B. Leistedt, H. V. Peiris, R. H. Wechsler *et al.*, Mon. Not. R. Astron. Soc. **461**, 1431 (2016).
[57] A. Porredon *et al.* (to be published).
[58] T. M. C. Abbott *et al.* (DES Collaboration), Phys. Rev. D **98**, 043526 (2018).
[59] N. MacCrann *et al.*, Mon. Not. R. Astron. Soc. **480**, 4614 (2018).
[60] W. D. Goldberger and I. Z. Rothstein, Phys. Rev. D **73**, 104029 (2006).
[61] L. Senatore, J. Cosmol. Astropart. Phys. 11 (2015) 007.
[62] D. Baumann, A. Nicolis, L. Senatore, and M. Zaldarriaga, J. Cosmol. Astropart. Phys. 07 (**2012**) 051.
[63] A. Chudaykin and M. M. Ivanov, J. Cosmol. Astropart. Phys. 11 (2019) 034.
[64] R. Takahashi, M. Sato, T. Nishimichi, A. Taruya, and M. Oguri, Astrophys. J. **761**, 152 (2012).

[65] T. Baldauf, L. Mercolli, and M. Zaldarriaga, Phys. Rev. D **92**, 123007 (2015).
[66] J. E. McEwen, X. Fang, C. M. Hirata, and J. A. Blazek, J. Cosmol. Astropart. Phys. 09 (**2016**) 015.
[67] X. Fang, J. A. Blazek, J. E. McEwen, and C. M. Hirata, J. Cosmol. Astropart. Phys. 02 (**2017**) 030.
[68] M. Schmittfull, Z. Vlah, and P. McDonald, Phys. Rev. D **93**, 103528 (2016).
[69] M. H. Qenouille, Biometrika **43**, 353 (1956).
[70] J. Tukey, Ann. Math. Stat. **29**, 614 (1958).
[71] P. Norberg, C. M. Baugh, E. Gaztanaga, and D. J. Croton, Mon. Not. R. Astron. Soc. **396**, 19 (2009).
[72] O. Friedrich, S. Seitz, T. F. Eifler, and D. Gruen, Mon. Not. R. Astron. Soc. **456**, 2662 (2016).
[73] J. Hartlap, P. Simon, and P. Schneider, Astron. Astrophys. **464**, 399 (2006).
[74] S. D. Landy and A. S. Szalay, Astrophys. J. **412**, 64 (1993).
[75] M. Jarvis, G. Bernstein, and B. Jain, Mon. Not. R. Astron. Soc. **352**, 338 (2004).
[76] J. Zuntz, M. Paterno, E. Jennings, D. Rudd, A. Manzotti, S. Dodelson, S. Bridle, S. Sehrish, and J. Kowalkowski, Astron. Comput. **12**, 45 (2015).
[77] E. Krause *et al.*, arXiv:1706.09359.
[78] O. Friedrich *et al.* (to be published).